

Score-matching neural networks for improved multi-band source separation

Matt L. Sampson^{1a}, Peter Melchior^{1a,b}, Charlotte Ward^{1a}, Sufia Birmingham^{1a}

^aDepartment of Astrophysical Sciences, Princeton University, Princeton, 08544, NJ, USA

^bCenter for Statistics and Machine Learning, Princeton University, Princeton, 08544, NJ, USA

Abstract

We present the implementation of a score-matching neural network that represents a data-driven prior for non-parametric galaxy morphologies. The gradients of this prior can be included in the optimization routine of the recently developed multi-band modeling framework SCARLET2, a redesign of the SCARLET method currently employed as deblender in the pipelines of the HyperSuprimeCam survey and the Rubin Observatory. The addition of the prior avoids the requirement of non-differentiable constraints, which can lead to convergence failures we discovered in SCARLET. We present the architecture and training details of our score-matching neural network and show with simulated Rubin-like observations that SCARLET2 outperforms SCARLET in accuracy of total flux and morphology estimates, while maintaining excellent performance for colors. We also demonstrate significant improvements in the robustness to inaccurate initializations. SCARLET2 is written in python, extended by jax and equinox, and is fully GPU compatible. The implementation and data package of the score model are publicly available at <https://github.com/pmelchior/scarlet2>.

Keywords: methods: machine learning, data analysis, techniques: image processing

1. Introduction

Upcoming astronomical surveys will produce huge amounts of data, with current estimates for the Rubin Observatory Legacy Survey of Space and Time (LSST; Ivezić et al., 2019) yielding on the order of 10 billion galaxies. This vast amount of data is meant to greatly reduce the statistical uncertainty of cosmological and astrophysical parameters. LSST specifically covers about half the sky to a limiting magnitude of $i \approx 27$. While detecting and measuring more faint and distant galaxies than ever before, this sensitivity increase will also drastically increase the occurrence of overlap between neighboring sources, a systematic effect known as *blending*. Galaxy blending has already been shown to affect up to 60% of galaxies in the HyperSuprime Cam (HSC) wide survey (Bosch et al., 2018) that has a limiting magnitude of $i \approx 26$. Blending thus constitutes a leading systematic issue in gravitational lensing and galaxy clustering studies (Mandelbaum, 2018; Melchior et al., 2021; Nourbakhsh et al., 2022). Therefore, accurate and computationally efficient deblending of galaxies, or an effective calibration

scheme that captures the effects of blending (MacCrann et al., 2022), is crucial to allow us to maximize the value of upcoming astronomical surveys. We pursue the former approach so as to minimize the efforts that may still be required for the latter.

There are a variety of publicly available deblending codes, including SExtractor (Bertin and Arnouts, 1996), the SDSS deblender (Lupton, 2005) and MUSCADET (Joseph et al., 2016), and SCARLET (Melchior et al., 2018). Methods based on neural network, usually trained on simulated or reliably unblended galaxies, have recently also shown good performance (e.g. Reiman and Göhre, 2019; Burke et al., 2019; Boucaud et al., 2020; Arcelin et al., 2021; Hemmati et al., 2022; Wang et al., 2022). In this work, we combine the strengths of the SCARLET method, which is currently implemented in the pipelines for HSC and LSST, with the flexibility of neural networks.

We describe the motivation for this change as well as the neural network architecture we choose in Section 2. In Section 3 we demonstrate the capability of the neural network to represent galaxy morphologies. We compare the performance of SCARLET and with the neural-network enhanced SCARLET2 on real and simulated data in Section 4, and summarize our findings in Section 5.

Email addresses: matt.sampson@princeton.edu (Matt L. Sampson^{1a}), peter.melchior@princeton.edu (Peter Melchior^{1a,b})

2. Methodology

2.1. Source separation

SCARLET separates and reconstructs astronomical sources in *multi-band* images through a generalized method of non-negative matrix factorization termed Constrained Matrix Factorization, where for every source k one factor, \mathbf{A}_k , refers to the spectral energy distribution across bands and the other, \mathbf{S}_k , to the intensity variation across the sky. An astronomical scene with a hyperspectral cube \mathbf{Y} is model as a linear combination of multiple sources,

$$\mathbf{Y} = \sum_k \mathbf{A}_k \times \mathbf{S}_k. \quad (1)$$

In this method, physically motivated parameter constraints are added to the optimization routine by means of proximal operators (Combettes and Pesquet, 2008, 2009; Parikh and Boyd, 2014) to ensure that the individual deblended sources appear realistic (see sec 2.3 of Melchior et al., 2018; Moolekamp and Melchior, 2018; Melchior et al., 2019, for details). Doing so is necessary for source separation or other ill-defined inverse problems because the likelihood function alone cannot distinguish between the many degenerate solutions that arise with overlapping galaxies, most of which will not look like galaxies. In SCARLET source constraints ensure that the reconstructed pixel value never falls below zero and that the radial profile decreases monotonically. This method is fast and provides a robust and effective non-parametric galaxy model, but many galaxies may have locally non-monotonic behavior, e.g. for tightly wound spiral arms. A more flexible model would be beneficial to better capture such features.

The inflexibility of those constraints occasionally even leads to unrealistic features, such as radial streaks, that formally satisfy the constraints. Such issues originate in the proximal gradient method, which finds the minimizer of $f(\mathbf{x}) + g(\mathbf{x})$, where f is a convex, differentiable function, in our case the negative log-likelihood function, and g is a regularizer, by the sequence

$$\mathbf{x}^{t+1} \leftarrow \text{prox}_{\lambda^t g}(\mathbf{x}^t - \lambda^t \nabla f(\mathbf{x}^t)) \quad (2)$$

with step sizes λ^t . For a non-differentiable regularizer, its proximal operator $\text{prox}_{\lambda g}$ amounts to a projection onto the surface of the manifold that satisfies the constraint, a so-called “subgradient”. If the gradient vector is directly opposed to the subgradient, this sequence leads to very slow convergence or even to a trapping of the optimizer in locations with very large f (see Figure 1 for a sketch).

These problems arise in practice. We found SCARLET to be vulnerable to getting trapped if, due to a bad initialization, the galaxy model requires large changes in the overall flux of a source, which leads to gradients with pronounced oscillating ring-like patterns and thus reconstructions with negative pixel values. But these are not allowed for non-negative models and therefore rejected by the proximal operator $\text{prox}_+(\mathbf{x}) = \max(\mathbf{x}, 0)$. The most direct gradient path is thus blocked (see Figure 7 for an example and Section 4.4 for a discussion of this failure mode). It is important to realize that the proximal projection is applied after every gradient step, so that this trapping can occur *during* the optimization even if the final model would satisfy the constraints because an intermediate model might violate them.

Lastly, non-differentiable regularizers also preclude most continuous methods, e.g. to determine parameter uncertainties through second derivatives of the log-likelihood function, or sampling methods. We thus seek to replace proximal optimization of the constrained likelihood,

$$L(\mathbf{x}) = \log \mathcal{L}(\mathbf{x} | \mathcal{D}) + g(\mathbf{x}), \quad (3)$$

with regular optimization of the Bayesian posterior,

$$L(\mathbf{x}) = \log \mathcal{L}(\mathbf{x} | \mathcal{D}) + \log \mathcal{P}(\mathbf{x}), \quad (4)$$

wherein the prior distribution $\mathcal{P}(\mathbf{x})$ takes the place of the constraints. In this work we focus on priors on galaxy morphologies \mathbf{S}_k .

2.2. Model for the prior distribution

Score-matching diffusion models are a class of generative deep learning models that produce high-quality sample images from a prior distribution. This is achieved through a neural network that is trained to approximate the gradient of the logarithmic prior distribution $\nabla \log \mathcal{P}(\mathbf{x})$, also known as the *score function*. There has been a great amount of work recently with these types of models, primarily in the domain of generative image modeling (Song and Ermon, 2019; Song and Ermon, 2020; Ho et al., 2020; Song et al., 2020; Nichol and Dhariwal, 2021) as well as adaptations to astronomy to generate realistically looking galaxies (Smith et al., 2022).

We utilize the same architecture presented in Song et al. (2020) and use the same loss function with minimal alterations. In this implementation of a diffusion model, the intended goal is to attain a solution to the Itô stochastic differential equation (SDE), called the *forward process*,

$$d\mathbf{x} = \mathbf{f}(\mathbf{x}, t)dt + g(t)d\mathbf{w}, \quad (5)$$

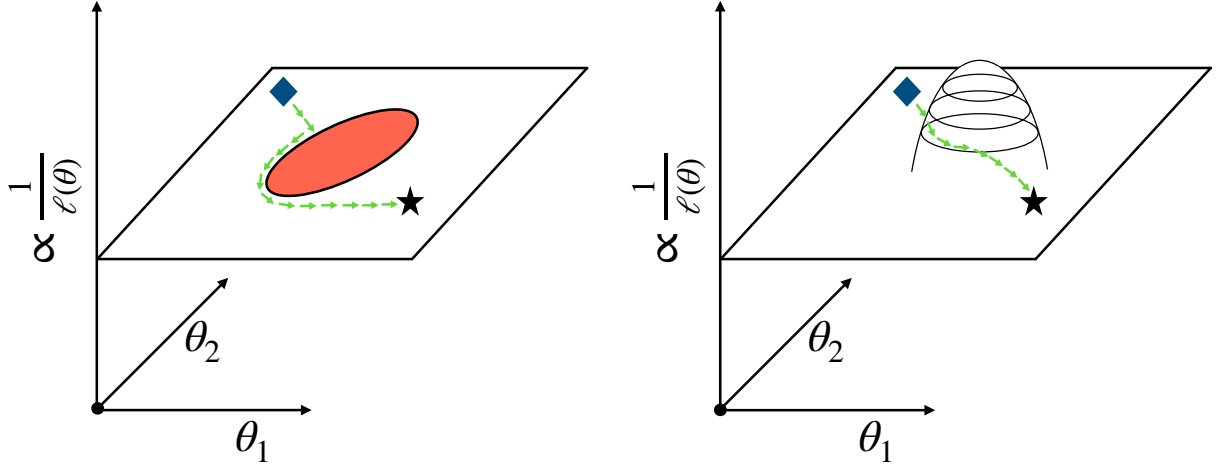


Figure 1: Sketch of optimization paths. SCARLET (*left*) uses constrained optimization to enforce physically desirable heuristics for galaxies, such as non-negativity and monotonic radial profiles, by proximal projections, which prevent the optimizer from taking steps through infeasible regions, slowing down or even impeding convergence. SCARLET2 (*right*) uses data-driven priors, which provide a continuous and fully differentiable posterior surface.

where $\mathbf{x} \sim \mathcal{P}(\mathbf{x})$ is a sample from the data-generating process, \mathbf{f} is a deterministic drift function, and \mathbf{w} is a sample from a standard Wiener process. For any time $t \in [0, T]$, the forward diffusion process amounts to a mean drift and an increasing addition of noise, both of which can easily be simulated. Anderson (1982) proved the existence of an analytical form to reverse Equation 5 as

$$d\mathbf{x} = \left[\mathbf{f}(\mathbf{x}, t) - g^2(t) \nabla \log \mathcal{P}_t(\mathbf{x}) \right] dt + g(t) d\bar{\mathbf{w}}, \quad (6)$$

where \mathcal{P}_t is the *time-dependent* form of the prior distribution and $\bar{\mathbf{w}}$ is again a standard Wiener process sample. In other words, when starting with noisy samples $\mathbf{x}(T) \sim \mathcal{P}_T(\mathbf{x})$ and reversing the diffusion, we can sample from $\mathbf{x}(0) \sim \mathcal{P}(\mathbf{x})$, our desired target distribution. Intuitively, any well-guided attempt of removing noise from the result of a diffusion process requires knowledge of the distribution of likely samples.

Equation 6 requires the evaluation of $\nabla \log \mathcal{P}_t(\mathbf{X})$, which we seek to accelerate by training a neural network s_θ on the following loss:

$$L(\theta) = \mathbb{E}_{\mathbf{x}(0)} \mathbb{E}_{\mathbf{x}(t)|\mathbf{x}(0)} \left(\left\| s_\theta(\mathbf{x}(t), t) - \nabla_{\mathbf{x}(t)} \log \mathcal{P}_{0t}(\mathbf{x}(t) | \mathbf{x}(0)) \right\|_2^2 \right). \quad (7)$$

The specific form of the time-dependent prior depends on \mathbf{f} and g . Song et al. (2020) demonstrated excellent

performance for a sequence of noise scales $\beta(t)$ with

$$\begin{aligned} \mathbf{f}(\mathbf{x}, t) &= -\frac{1}{2}\beta(t)\mathbf{x} \text{ and} \\ g(t) &= \sqrt{\beta(t)(1 - e^{-2\int_0^t \beta(s)ds})}, \end{aligned} \quad (8)$$

which leads to the time-dependent prior

$$\begin{aligned} \mathcal{P}_{0t}(\mathbf{x}(t) | \mathbf{x}(0)) &= \mathcal{N}(\mathbf{x}(t) | \mathbf{m}(t), \mathbf{V}(t)) \text{ with} \\ \mathbf{m}(t) &= \mathbf{x}(0) e^{-\frac{1}{2}\int_0^t \beta(s)ds} \text{ and} \\ \mathbf{V}(t) &= \mathbf{I} - e^{-\int_0^t \beta(s)ds} \mathbf{I}. \end{aligned} \quad (9)$$

Once the integral $\int_0^t \beta(s)ds$ is evaluated, the gradients of logarithm of this prior can be analytically calculated and inserted in Equation 7 to train the score-matching diffusion model s_θ .

3. Diffusion model training

We train our neural network model to reverse the diffusion process from the arbitrary start point of $T = 10$ until to the zero-temperature (sometimes *zero-time*) end point of $t = 0$. A demonstration of this process is shown in Figure 2, and the details of the training process are described below.

3.1. Datasets

For our initial training set of galaxies we used the recent source catalog from HSC. SCARLET has already been

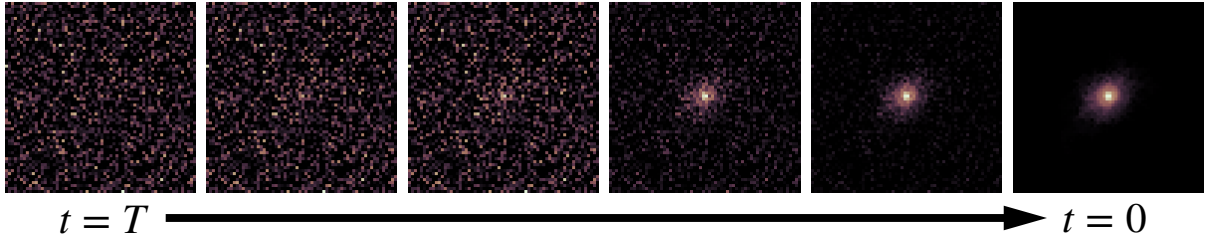


Figure 2: Sample from the HSC galaxy morphology prior. The left most panel shows the initial random Gaussian noise field, from which noise is removed step by step. The final denoised image at time $t = 0$ is then a sample consistent with the data distribution.

run on the entirety of this catalogue, we therefore have direct access to the deblended sources. We extracted around 250,000 sources from each patch for three tracts {9615, 9697, 9813}. The sources are centered in their respective images, with image dimensions ranging from 15×15 to 221×221 pixels. For our diffusion model, we decided to train on only 2 sizes, *low resolution* of size 32×32 and *high resolution* 64×64 . For images larger than 64×64 , there are far fewer observations, and at these resolutions galaxies are usually highly significant and therefore rarely need to regularization from a prior. To construct our two training sets we use zero-padding around the edges of the original source images.

We also train a model on a mock catalogue of Zwicky Transient Facility (ZTF) like observations (Bellm et al., 2019; Graham et al., 2019; Dekany et al., 2020). For this, we create a range of isolated galaxies using `GalSim` (Rowe et al., 2015) Sersic profiles of $n = 1$ (exponential profile) and $n = 4$ (De Vaucouleurs profile). We vary four morphological parameters of the simulated galaxies: the radius, axis ratio, rotation angle, and sub-pixel shift from image center, with probabilities determined by the distribution of host galaxy properties from the sample of 1626 variable AGN in ZTF presented in Ward et al. (2023). We simulate 10,000 galaxies (5,000 galaxies for both Sersic flux profiles) each in two box sizes of 32^2 and 64^2 pixels. With this procedure, we demonstrate the application of data-driven priors for special analyzes (see Section 6.1) with a very modest training data set.

3.2. Data transformation

The majority of our training data for both the HSC and the mock ZTF images often comprise of only a small amount of bright pixels in the central region of the image, with the rest of the image being close to zero. To enhance the low brightness pixels, we applied a transformation

$$h(\mathbf{x}) = \frac{\log(\mathbf{x} + 1)}{0.1}, \quad (10)$$

which we found to result in increased model performance, especially for faint galaxy features. To undo this transform, and ensure that the gradient used in SCARLET’s optimisation routine is in the same coordinates of the observation, we add the Jacobian of the transformation to the score function,

$$\nabla \log P_{\mathbf{x}} \rightarrow \nabla \log P_{\mathbf{x}} \cdot \mathbf{J}(h), \quad (11)$$

where the calculation of the Jacobian of $\mathbf{J}(h)$ is done by automatic differentiation in `jax`.

3.3. Generative capabilities

An example of the trained diffusion process is shown in Figure 2, which is based on the HSC prior. The denoising process takes place over an arbitrary time period $t = T \rightarrow t = 0$, with a noticeable galaxy center appearing approximately halfway into the process. Additional diffusion-model generated examples for both image sizes are shown in Figure 3. Visually, there is no discrepancy between the generated samples and the training data, consistent with other studies showing the successful performance of diffusion models to generate realistic galaxy images (Smith et al., 2022; Adam et al., 2022).

3.4. Out-of-domain performance

Our model is trained to generate the gradients of a log-prior distribution of individual galaxies. One would therefore expect that, when shown images of objects that clearly deviate from the galaxy samples, the gradient field would seek to suppress features that are unlike those seen in galaxies. To test this, we take the generated sample from Figure 2 and add an artifact in the form of a ring around the galaxy, as shown in the top row of Figure 4. We then evaluate the score function on both the original and altered image, which is shown in the bottom row of Figure 4. The gradients are evaluated at the zero-temperature point ($t = 0$) because that corresponds to the gradient field of the final denoised

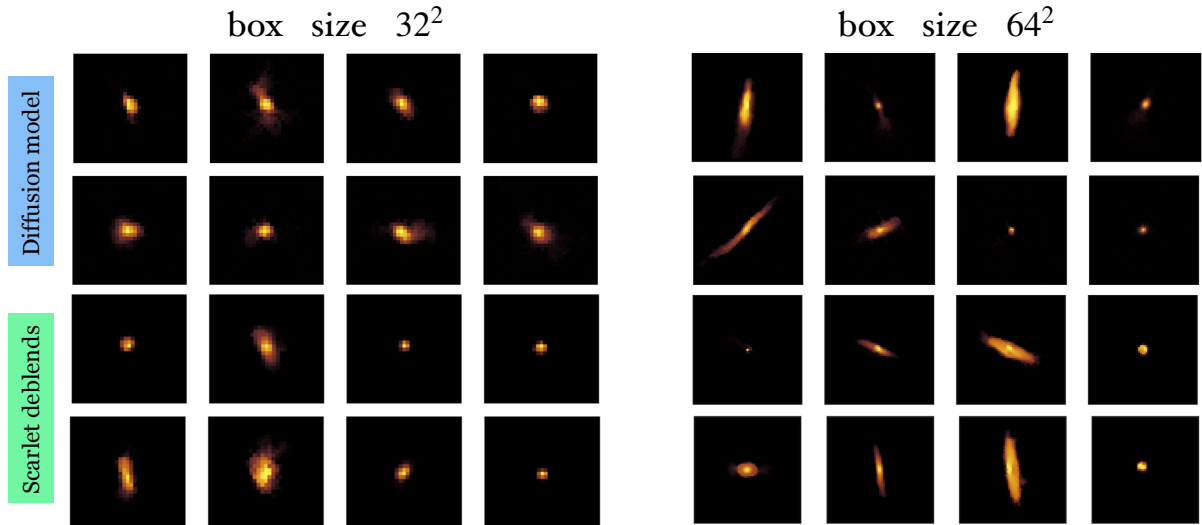


Figure 3: Comparison between generated samples, and randomly chosen samples from the training set for both size 32^2 and 64^2 images.

sample. We see in the gradients of the unaltered image that there is no clear structure, which is expected as this image represents a direct sample from the prior.

In the image with the artifact, we clearly see that the ring feature is strongly suppressed by the prior with high negative values in the gradients at the precise location of the ring.

This tests demonstrates not only that the data-driven galaxy prior is useful to render the models robust to artifacts but also that the main features of the gradient are stable to tests outside of the training domain. The ability to suppress out-of-domain features should be particularly useful for source separation tasks, where the light contamination of a nearby source will appear atypical given the *isolated* galaxies in our training data.

4. Prior-informed source separation

To deblend sources, SCARLET employs a first-order gradient optimization scheme, which computes the gradients of the loss function Equation 3 with an explicit likelihood, e.g. for uncorrelated Gaussian noise,

$$\log \mathcal{L} = -\frac{1}{2} \left\| \mathbf{W} \cdot \left(\mathbf{Y} - \mathbf{P} \sum_k \mathbf{A}_k \times \mathbf{S}_k \right) \right\|_2^2, \quad (12)$$

where \mathbf{Y} is a multi-band image cube, \mathbf{W} the inverse variance weights in every pixel, and \mathbf{P} is a, typically linear, forward operator that describes the instrument response. Following the approach of (Lanusse et al., 2019), SCARLET2 optimizes Equation 4, which maintains the likeli-

hood gradient and thus a full forward model of the instrument, and adds priors for any source morphology \mathbf{S}_k :

$$\nabla_{\mathbf{S}_k} L = \nabla_{\mathbf{S}_k} \log \mathcal{L}(\mathbf{A}_1, \dots, \mathbf{A}_K, \mathbf{S}_1, \dots, \mathbf{S}_K | \mathbf{Y}) + s_\theta(\mathbf{S}_k) \quad (13)$$

While one could add additional priors to the source SEDs, morphologies exhibit usually more degeneracies in the region of source overlap, so that morphology priors are more critically needed.

To be clear, we only evaluate the score function s_θ for each \mathbf{S}_k , not the prior value itself, as doing the latter would be very costly. We therefore do not obtain an estimate of the log-posterior value, but we can be assured that by following these gradients (either through gradient descent or in a Hamiltonian Monte Carlo approach) we find the maximum of (or sample from) the posterior.

4.1. Zero-temperature evaluation

Running a full diffusion model to sample from the data distribution is computationally costly as it often requires hundreds of calls to the score function. However, for our purposes, we only wish to call an evaluation of the score function at $t = 0$, i.e. the gradient of the original data distribution. If possible, doing so would save significant computation costs, but the entire development of diffusion model was motivated by the insight that such zero-temperature gradients are usually inaccurate (Song and Ermon, 2019). So, why do we believe that we can get away with it? Because 1) galaxy morphologies are not nearly as complex as natural images which form the usual test cases and have shown to

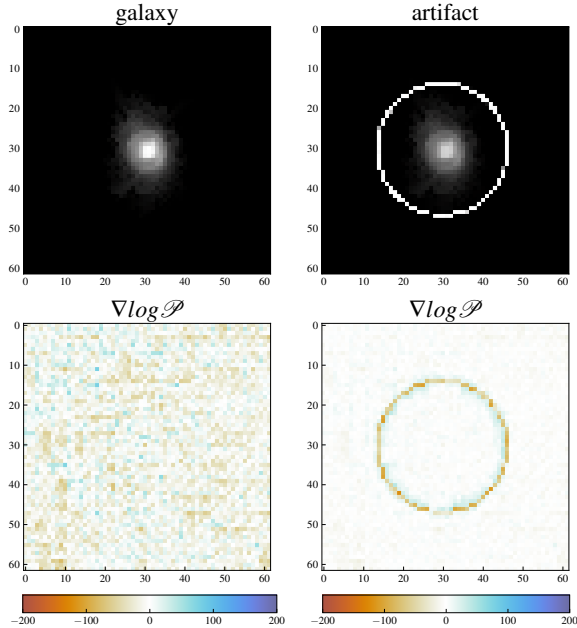


Figure 4: Artifact removal. A galaxy sampled from our morphology prior (*top left*) shows flat prior gradients (*bottom left*), but an added ring artifact (*top right*) causes large gradients that seek to suppress the features that do not occur in the training data (*bottom right*).

noticeably benefit from the diffusion process, and 2) we initialize each source with a reasonable first guess to the true morphology shape, so that we usually stay close to the range of examples the score-model has been trained on. Figure 4 even demonstrates that out-of-distribution artifacts have valid zero-temperature gradients, which implies that argument 1) above is more important than argument 2), which inspires our initial confidence that a full diffusion process would be mostly unnecessary for source separation of the majority of galaxies in large survey. However, we will now test this approach and note that a full diffusion model might be required for more complicated morphologies.

4.2. Example

We run SCARLET2 with the neural network prior on an example scene from the HSC dataset shown in Figure 5, where we the HSC pipeline found four distinct peaks. The reconstructions for these sources, the entire scene with PSF convolution, and the residuals are shown in the top row of Figure 5. We see that there are three strongly blended sources (0, 1, and 3), while source 2 is mostly isolated. Rows 2–5 of Figure 5 show, in separate columns, the individual reconstructions of each source, the PSF-convolved source, the observation, and the spectral energy distribution (SED) of the

source, respectively. Despite the strong overlap, each source morphology appears realistic, free of artifacts, and contributes to a high-fidelity reconstruction of the entire scene. For this examples, SCARLET2 required 88 iterations to converge to a relative error tolerance of 10^{-4} which took ~ 3 seconds.

4.3. Ground truth testing

While it is nice to know that SCARLET2 yields realistic results, we want to know if it yields *accurate* results. We now test the performance of the prior-informed model from SCARLET2 and compare it with models of the same simulated scenes from SCARLET. We employ three performance metrics for flux, morphology and SED recovery: the relative error on the absolute flux

$$e_F = \frac{(f - f_{\text{true}})}{f_{\text{true}}}, \quad (14)$$

where f is the total flux of the scene, $f = \sum_b^{\text{bands}} \sum_i^{\text{pixels}} \mathbf{Y}_{b,i}$, and the correlation coefficient

$$\xi_v = \frac{v_{\text{true}} \cdot v}{\sqrt{v_{\text{true}} \cdot v_{\text{true}} \cdot v \cdot v}}, \quad (15)$$

where $v = \mathbf{S} \equiv \sum_b^{\text{bands}} \mathbf{Y}_{b,i}$ denotes the morphology correlation and $v = \mathbf{A} \equiv \sum_i^{\text{pixels}} \mathbf{Y}_{b,i}$ the SED correlation, respectively.

We create a mock catalog of 2,000 LSST-like blended images with the BLENDINGTOOLKIT (Mendoza), which is based on the heavily tested GALSIM framework (Rowe et al., 2015). We chose a maximum magnitude of $i \leq 27$ and between 2 to 8 sources for each blend. Following Melchior et al. (2018), we plot our metrics as a function of the true source flux or the blendedness

$$\beta_k = 1 - \frac{\mathbf{S}_k \cdot \mathbf{S}_k}{\mathbf{S} \cdot \mathbf{S}_k}, \quad (16)$$

where k represents the k -th component of the scene, \mathbf{S}_k its morphology images, and $\mathbf{S} = \sum_k \mathbf{S}_k$, all of which are computed from the truth images.

One would expect that fainter, and/or more blended sources will have less accurate reconstructions, and, indeed, Figure 6 show these main trends. More importantly, in both the flux (top rows) and morphology (middle rows) we see a clear improvement in accuracy when using SCARLET2 OVER SCARLET. The differences are most pronounced in regions of low total flux (left side of left panels in Figure 6), and high degrees of blending (right side of right panels in Figure 6). The SED accuracy is very similar across both codes, which is not entirely surprising because consistent colors can be found regardless of the assumed morphology.

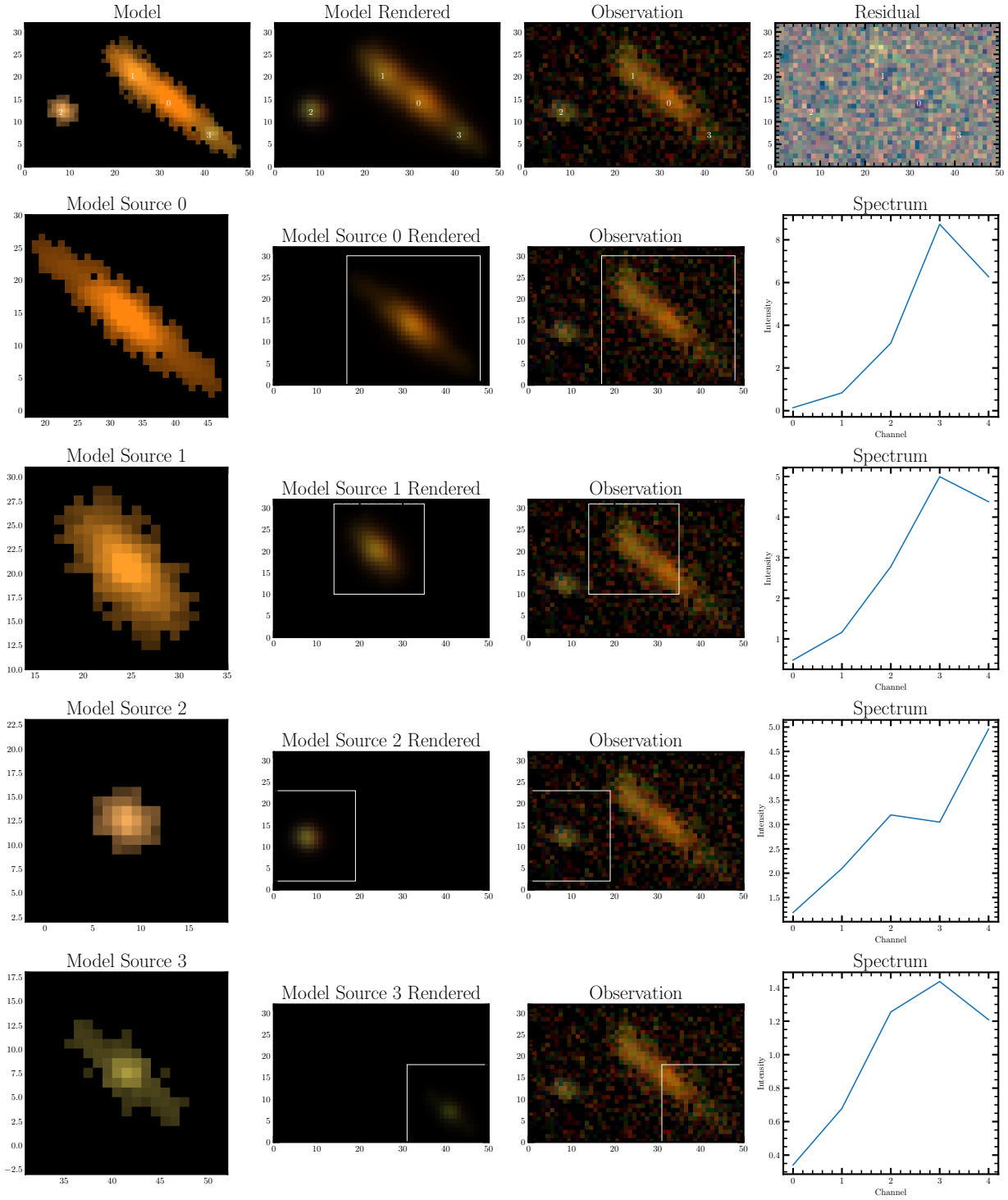


Figure 5: Example deblending. *Top row, left to right*: SCARLET2 reconstructed scene without PSF, convolved with the PSF, the HSC observation, and the residuals. *Rows 2–5, left to right*: the individual model for each source, its contribution to the PSF-convolved scene, the location in the observation, and its SED.

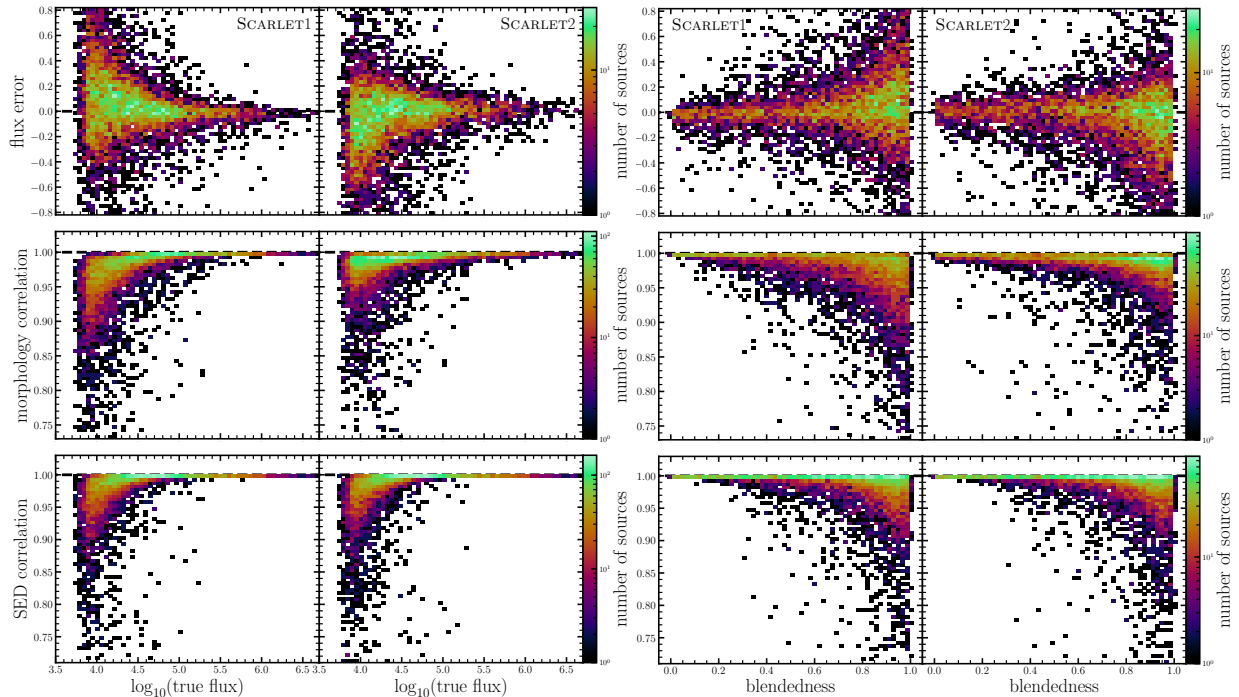


Figure 6: Comparison of deblending performance between SCARLET and SCARLET2. From top to bottom: the relative error of total fluxes as calculated by Equation 14, the correlation coefficient as defined in Equation 15 for the morphology, and the correlation coefficient for the SED.

4.4. Robustness to initialization

Due to the nature of the deblending problem, the surface of the loss function is highly non-convex. This means that optimizers are in general sensitive to specific hyper-parameters and initializations. As explained in Section 2, the proximal optimization of SCARLET is expected to be more vulnerable because paths through infeasible regions are impossible. To enable, as best as possible, convergence to a reliable model, it therefore may be necessary to have a good initialization of the source models. However, in blends sufficiently good initialization may be impossible and, even when done well, finding the optimal solution is still not guaranteed. It is therefore critical to have the sources models be robust to inaccurate initialization.

Figure 7 shows the results of the source reconstruction of models with intentionally poor initializations for the multi-band spectrum or the morphology. Specifically, we take the observation shown in the leftmost panels, and use SCARLET to estimate the spectrum and morphology of each identified source. We also run SCARLET2 with the same initialization as SCARLET. The models are shown in the top two rows of Figure 7.

We then multiplied the spectrum values by a factor of 10, resulting in an artificially bright initialization. We

see in the row 3 of Figure 7 that SCARLET performs poorly in this setup, with obvious errors in the models and overall a poor fit to the data. While the scenario appears contrived, thus failure mode has been observed in practice when users unintentionally provided wrong flux estimates. SCARLET2 fares much better when confronted with such a poor initialization and produces models that are virtually indistinguishable from the earlier better initialization (row 4). Even with a flat spectrum initialization, the SCARLET2 model is still practically unchanged. All trials were run for 200 iterations. But we point out that running for even more iterations would not have improved the SCARLET models, demonstrating that the proximal optimizer is indeed trapped, not just slower than the prior-augmented version.

For a more rigorous analysis of the robustness to SED initializations, we also run the test of Section 4.3, but this time with the initialization for the SED set to 20 times the initial value calculated by SCARLET. We again allow for both SCARLET and SCARLET2 to run for up to a maximum of 200 iterations, with a relative step size taken for both the morphology and SED parameters which results in the best case fitting for both deblending codes. Figure 8 shows the deblending accuracy metrics. We see quite notable differences in flux error, and

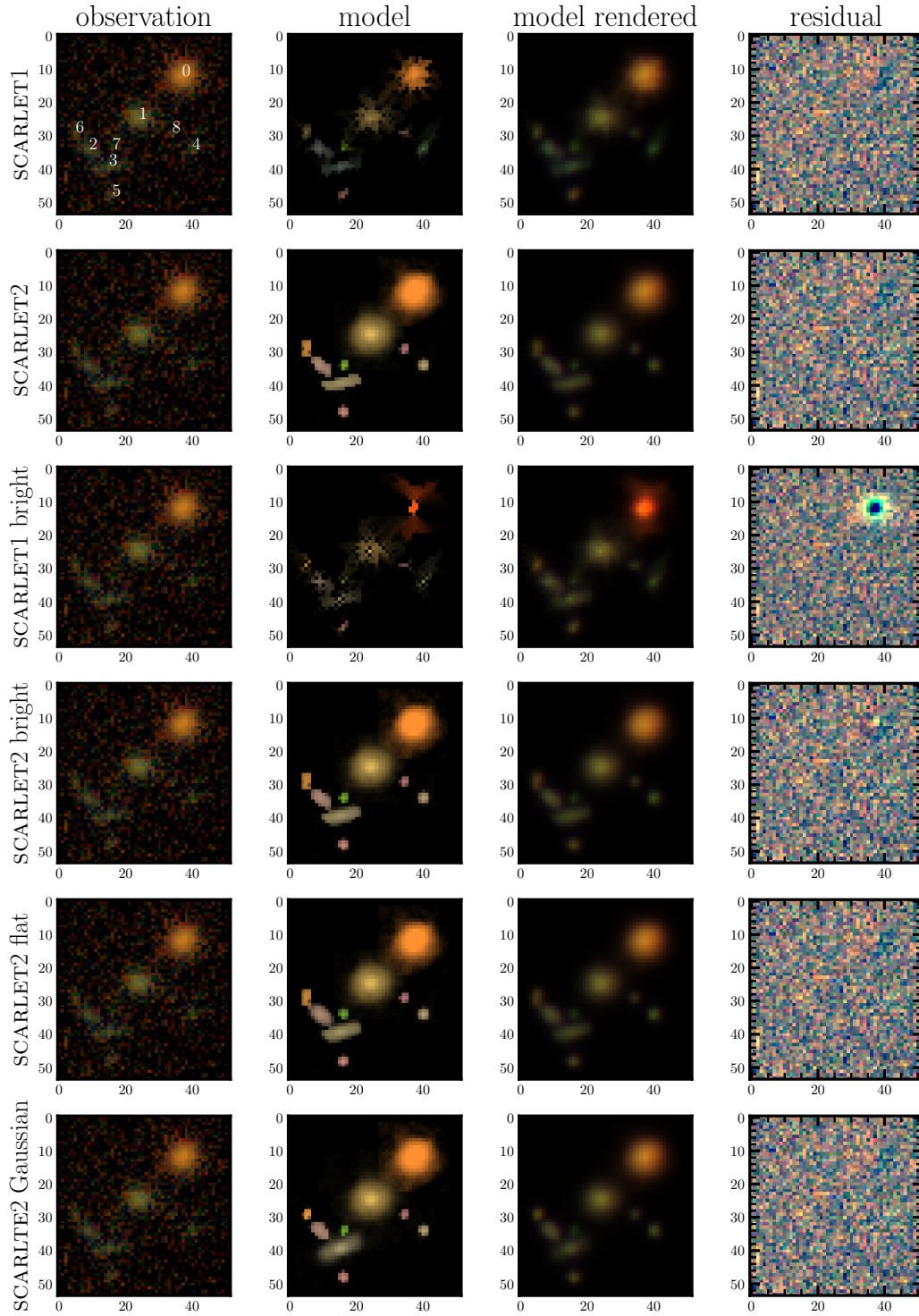


Figure 7: We show comparisons between the visual deblending performance of SCARLET 1 and 2 on a set observation. We change the initialization of the SED from its best-fit values (in **top 2 rows**) to 20 times brighter in each band (**rows 3 and 4**). In **row 5** we show results from initializing the spectrum of SCARLET2 with a flat array of ones for each band and **row 6** we show the result from initializing each source morphology with a 2D Gaussian.

morphology and SED correlations for the SCARLET trials, with large amounts of scatter around the optimal values for all metrics. Notably, even for bright and less blended sources, SCARLET struggles, with the SED correlation that never reach 1. This is the same problem seen in Figure 7, namely that sufficiently large changes in the overall flux lead to prominent errors in color and morphology. SCARLET2, on the other hand, does an excellent job recovering from these poor initializations: there is little difference between the performance of the deblender with a good and an intentionally bright SED initialization.

We also test the performance of SCARLET2 with random morphology initializations. SCARLET2 is ran once with the best fit initializations, and once with each source being initialized by a 2D Gaussian roughly 20% of the box size drawn around the center of each source. This is the same initialization used in row 6 of Figure 7. The results are shown in Figure 9 with the best-fit initializations in the left columns and the 2D Gaussians in the right. We see a mostly similar performance of both initializations, with the differences being most prominent at both the brightest and least blended, and faintest and most blended ends. The 2D Gaussian initialization performs well for faint and/or highly blended sources, which is most clear in the middle panels showing the morphology correlation. For brighter, less blended sources the best-fit initializations are marginally better for the morphology, however, this is not completely unexpected as these sources are likely to be larger, and less circular in shape, meaning the optimizer would need to do make larger changes when initialized with the Gaussian. Both trials have near identical results in the SED correlations. Interestingly, the flux of faint sources tends to be overestimates when using the Gaussian initializations, as compared to slightly underestimates with the best-fit model.

Due to the extra work required by the optimizer, we run the Gaussian initialized trials with a *cosine one-cycle* scheduler (Smith and Topin, 2017), as implemented in optax, which scales the step sizes taken. This allows for smaller initial steps during the initial phase when the confidence in the gradient direction is weaker, and larger steps during the middle stages of the optimization routine.

4.5. Robustness to choice of prior

Learning the prior is in itself complicated because one needs access to a sufficient number of deblended and deconvolved galaxy images that have the same properties as those found in the target observations. But

the availability and fidelity of such images is often limited, e.g. to regions with space-based data, where blending and PSF convolution can be ignored. In our case, we trained the prior on earlier SCARLET models of HSC observations. While usually very accurate, we know that SCARLET does not always obtain perfect deblended models, and there is a tendency for structures such as radial streaks to appear on the outsides of these models due to the limitations of proximal optimization. This begs the question how accurately the prior needs to be in order to be useful.

We test the performance of SCARLET2 on HSC-like examples, but with an ill-fitting prior, specifically, the ZTF prior discussed in Section 3.1. It was made from simulated galaxies with properties characteristic of brighter AGN hosts. Figure 10 shows the results of this test, where we observe very similar performance across the flux error and SED, with the morphology being slightly worse performing for bright and/or weakly blended sources when using the ZTF prior. This test demonstrates that good deblending can be achieved with SCARLET2 even if the prior is only approximately correct. We interpret this result as the prior providing some stability for the optimizer to choose and maintain broadly correct update directions, with the detailed inadequacy of the prior being hidden by the noise.

4.6. Quantifying hallucinations

An inevitable problem when using neural networks to solve inverse problems is the possibility of *hallucinations* appearing in the reconstructed images. In this context, hallucinations are defined as features in the reconstructed image that come directly from the prior as opposed to the data. Particularly in low SNR regions or regions of significant blending the constraining power of the data is severely limited, so that the posterior will necessarily be prior-dominated. While we have demonstrated in Section 4 that the addition of a prior improves the reconstruction of blended sources, it behooves us to provide a measure of (un)ambiguity of the results, i.e. we want to quantify what areas of the source model are constrained by the prior rather than the likelihood.

In Sampson and Melchior (2023), we presented a practical approach. In short, we define a *hallucination score* as

$$\Delta\mathbf{F} = \text{Diag}(\mathbf{F}_{\log\mathcal{P}}) - \text{Diag}(\mathbf{F}_{\log\mathcal{L}}), \quad (17)$$

where $\text{Diag}(\mathbf{F})$ is the diagonal of the Fisher information matrix, i.e. the negative Hessian of the logarithmic probability, calculated separately for the prior and the

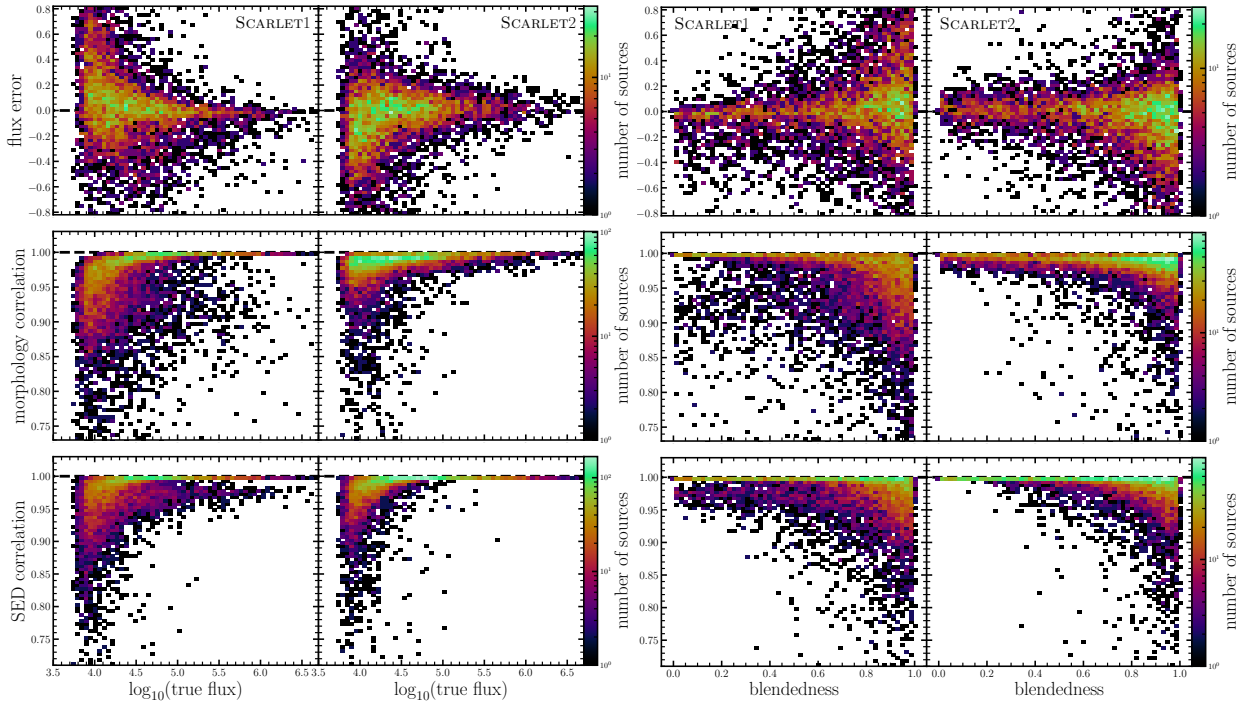


Figure 8: Same as Figure 6, but with the flux initialized too high by a factor of 20.

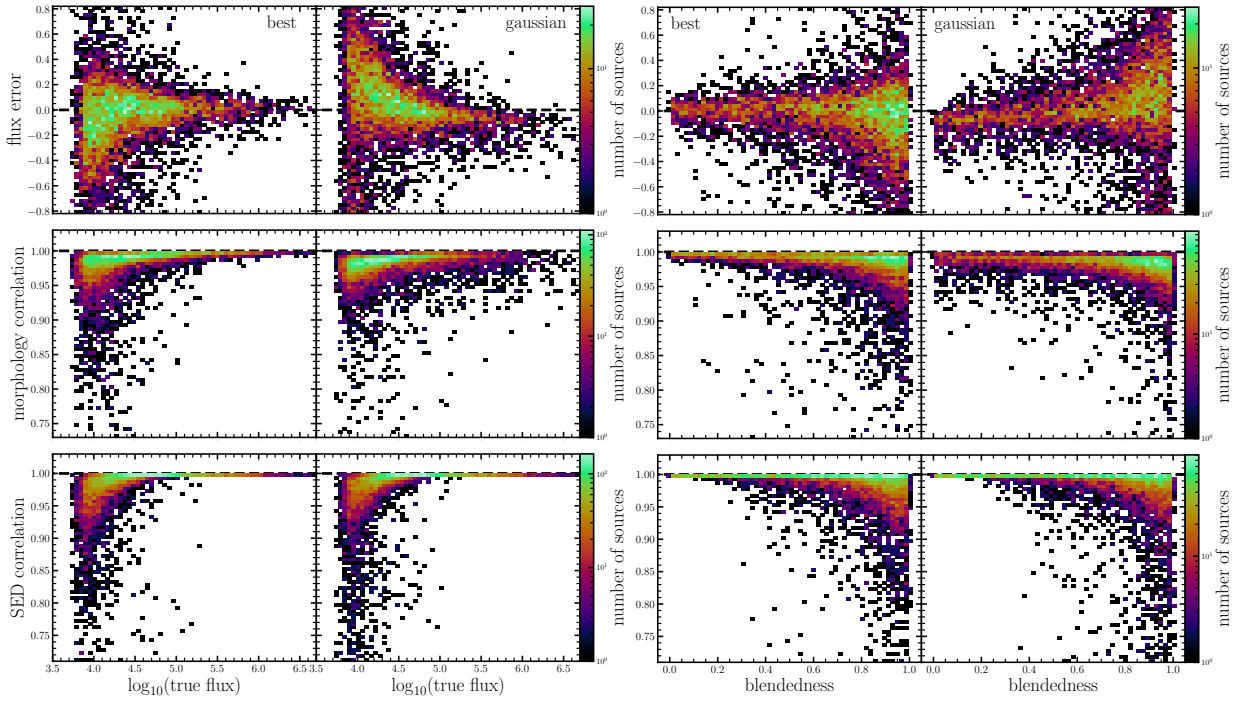


Figure 9: Same as Figure 6, but with the left columns of each 2 panels showing SCARLET2 with the best fit initialization, and the right with a 2D Gaussian.

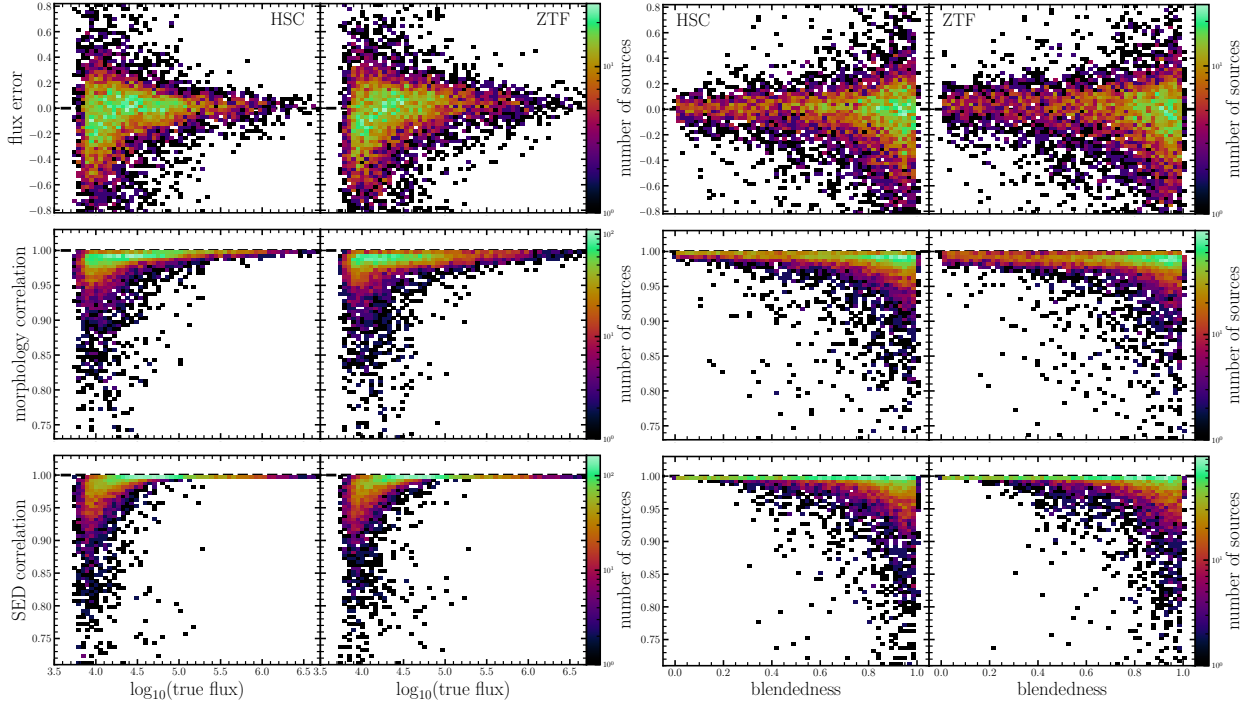


Figure 10: Same as Figure 6, but with the left columns of each 2 panels showing SCARLET2 with the HSC prior, and the right with a ZTF prior.

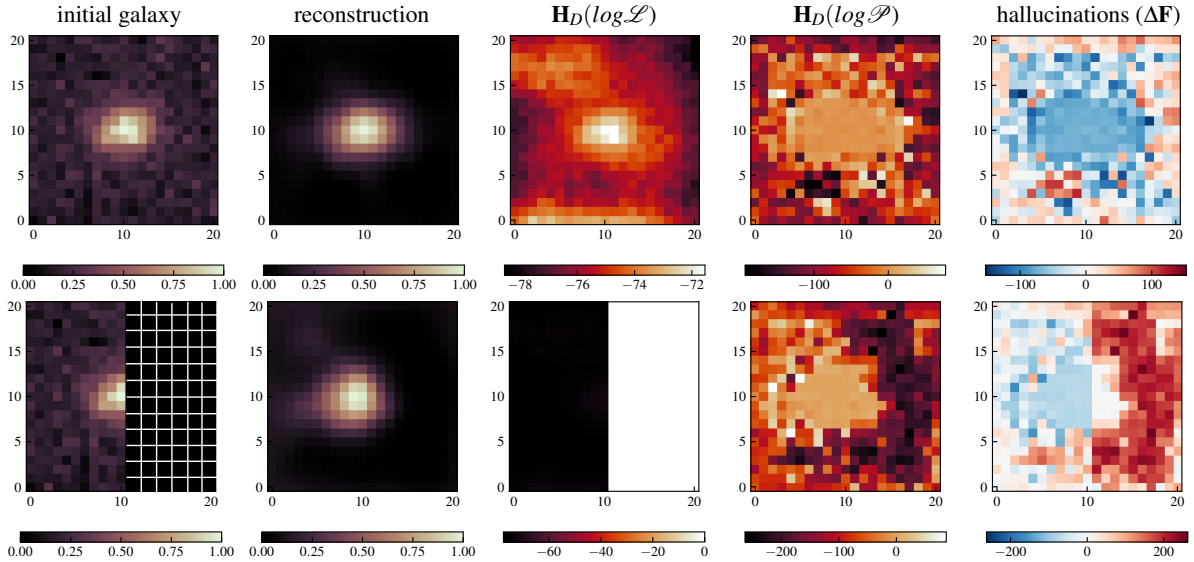


Figure 11: Hallucination score. The first two panels show the input images and the SCARLET2 models. Panels 3 and 4 show the Hessian diagonal for $\log \mathcal{L}$ and $\log \mathcal{P}$, respectively. We note the features of $\mathbf{H}_D(\log \mathcal{L})$ come directly from the variance weighting in the initial HSC data for the galaxy. The rightmost panel show the hallucination score $\Delta \mathbf{F}$ from Equation 17. The red shading indicates regions dominated by the prior, whereas the blue shading shows regions dominated by the likelihood. In the second row, the input image is identical, but the right half is masked out.

likelihood. While the Hessian of the latter can be computed with automatic differentiation, for the former we use Hutchison’s method to exploit that we already have the first derivatives in the form of the score model s_θ (see [Sampson and Melchior \(2023\)](#) for full details).

[Figure 11](#) shows an example of this method with the diagonal Hessians for both the likelihood and the prior, as well as the hallucination score. In the bottom row, we artificially set the value of the image weights in the right half of the scene to zero, meaning we have no information on the galaxy morphology in this region. As expected, the hallucination score of the second case reveals that the right side of the source model is strongly prior-dominated. In both cases, the outskirts of the galaxy model are more due to the prior than the inner regions where the data is more significant.

To form an overall prior-vs-likelihood metric, we define the scalar confidence

$$\gamma = -\Delta\mathbf{F} \cdot \mathbf{S}, \quad (18)$$

i.e. the hallucination score weighed with the morphology of the source, where brighter regions matter more for the fidelity of the model. The confidence γ can be seen as a generalization of conventional SNR measures because for isolated sources it scales with the significance of the data, and for blended sources it incorporates the uncertainty that is caused by the overlap through the contributions from the prior.

The calculation of the hallucination score and the confidence score is fully automated in `SCARLET2`, and can be requested by the users after the optimization whenever such a detailed analysis is warranted.

4.7. Runtime comparison

The sheer size of data associated with upcoming large surveys places a premium on computational efficiency of any deblending tool intended to be used at scale. Because `SCARLET` is already employed as deblender in the HSC and LSST pipelines, our aim for `SCARLET2` is that of comparable runtimes. The main differences lie in 1) a high cost for each evaluation of the score model, 2) just-in-time compilation of `SCARLET2` code, and 3) the ability to migrate `SCARLET2` code to GPUs, whereas `SCARLET` is limited to CPUs.

On CPU nodes, we find that for a typical case of five sources per image and 50 optimizer iterations `SCARLET2` takes ~ 3.9 times longer than `SCARLET`. When running for 200 iterations, the factor is reduced to ~ 1.5 , which is explained by the initial overhead and subsequent gains from just-in-time compilation. For a single

source and 50 iterations, `SCARLET2` takes almost an identical amount of time to run, which reveals the higher cost of score-model evaluations in `SCARLET2` compared to those of proximal operators in `SCARLET`. On average, from testing performed in [Section 4.4](#) and [Section 4.5](#) we find on average `SCARLET` takes $\sim 20 - 30$ steps to convergence when initialized with the best fit morphology and spectrum with `SCARLET2` taking ~ 50 for a relative error tolerance of 1×10^{-3} . When initialized poorly, `SCARLET` will often run to the max iteration set, while `SCARLET2` converged in ~ 100 iterations. More fine-tuning with optimizer parameters and scheduling may further reduce the iteration counts of `SCARLET2`.

On 40GB Nvidia A100 GPU of the NERSC cluster `Perlmutter`¹, a single source with 50 iterations runs on average are ~ 1.5 times faster than `SCARLET` on CPUs. For five sources, the GPU trials are ~ 3.5 and ~ 4 times faster than the CPU version for 50 and 100 iterations, respectively.

We can conclude that despite the additional score model evaluations for every source in every iteration, runtimes of `SCARLET2` are somewhat but not drastically slower than those of `SCARLET`. The results also suggest that running larger scenes with more sources should make good use of the processing power and large memory of modern GPUs.

5. Summary

We presented an implementation of non-parametric galaxy morphology priors by a diffusion model and demonstrate its efficacy for source separation in multi-band survey data such the upcoming LSST. This prior is integrated into a new version of the source modeling framework `SCARLET` ([Melchior et al., 2018](#)), dubbed `SCARLET2`, which is implemented in `jax` and `equinox`. The addition of priors has allowed for the removal of the proximal operator-based constraints, which `SCARLET` relies on to ensure physically reasonable properties of deblended sources. We performed a series of accuracy and benchmarking tests for this new code, with direct comparisons made to `SCARLET`. Our main results are:

- We find a significant improvement in the accuracy in total fluxes and morphology of deblended sources from a mock LSST dataset. The improvements are most notable in regions of either low total flux and/or highly blended sources.

¹<https://docs.nersc.gov/systems/perlmutter/architecture/>

- We find SCARLET2 to be very robust to inaccurate initialization. This is a significant improvement over SCARLET, whose proximal optimization is prone to convergence issues when poorly initialized.
- The inclusion of a data-driven prior allows for the probabilistic removal of artifacts or missing data from images. Compared to proximal projections, which simply disallow infeasible solutions, priors are more informative because they can differentiate between more and less likely image configurations.
- We find good performance of the deblending routine even when using slightly inadequate priors. This shows promise for the use of this method not only on large-scale surveys such as HSC and LSST, but also for any custom source separation tasks where the training data for the score model is limited in size or fidelity.
- We include an efficient method for determining a confidence metric of deblended sources based on the Hessians of the prior and the likelihood. This metric allows to identify regions of low confidence in deblended sources, or to automatically flag low confidence sources.
- The runtime of SCARLET2 with a score-matching model is broadly comparable to SCARLET. This can be attributed to just-in-time compilation and the zero-temperature evaluations of the score model, a massive computational gain justifiable only because galaxy morphologies follow distributions that are sufficiently easy to model. While slower by a factor of 3–4 for typical scenes on CPUs, SCARLET2 code can be run on GPUs and TPUs, and initial testing suggests comparable walltimes and the possibility of running larger scenes simultaneously.

SCARLET2 is being developed with the dual goal of enabling large-scale production runs for future surveys as well as custom investigations of smaller data sets. We make the code available for the wider astrophysical community at <https://github.com/pmelchior/scarlet2> and welcome comments and contributions. The trained score models used for this analysis are publicly available at <https://github.com/SampsonML/galaxygrad>.

Acknowledgments

M.L.S would like to thank Roohi Dalal for her helpful comments and discussion about the scientific applications of this work. M.L.S acknowledges funding from Princeton University’s first-year Fellowship in Natural Sciences.

References

- Adam, A., Coogan, A., Malkin, N., Legin, R., Perreault-Levasseur, L., Hezaveh, Y., Bengio, Y., 2022. Posterior samples of source galaxies in strong gravitational lenses with score-based priors, in: *Machine Learning and the Physical Sciences Workshop*, p. E1. doi:[10.48550/arXiv.2211.03812](https://doi.org/10.48550/arXiv.2211.03812), [arXiv:2211.03812](https://arxiv.org/abs/2211.03812).
- Anderson, B.D., 1982. Reverse-time diffusion equation models. *Stochastic Processes and their Applications* 12, 313–326.
- Arcelin, B., Doux, C., Aubourg, E., Roucelle, C., LSST Dark Energy Science Collaboration, 2021. Deblending galaxies with variational autoencoders: A joint multiband, multi-instrument approach. *Monthly Notices of the Royal Astronomical Society* 500, 531–547. doi:[10.1093/mnras/staa3062](https://doi.org/10.1093/mnras/staa3062), [arXiv:2005.12039](https://arxiv.org/abs/2005.12039).
- Bellm, E.C., Kulkarni, S.R., Graham, M.J., Dekany, R., Smith, R.M., Riddle, R., Masci, F.J., Helou, G., Prince, T.A., Adams, S.M., Barbarino, C., Barlow, T., Bauer, J., Beck, R., Belicki, J., Biswas, R., Blagorodnova, N., Bodewits, D., Bolin, B., Brinnet, V., Brooke, T., Bue, B., Bulla, M., Burruss, R., Cenko, S.B., Chang, C.K., Connolly, A., Coughlin, M., Cromer, J., Cunningham, V., De, K., Delacroix, A., Desai, V., Duev, D.A., Eadie, G., Farnham, T.L., Feeney, M., Feindt, U., Flynn, D., Franckowiak, A., Frederick, S., Fremling, C., Gal-Yam, A., Gezari, S., Giomi, M., Goldstein, D.A., Golkhou, V.Z., Goobar, A., Groom, S., Hacopians, E., Hale, D., Henning, J., Ho, A.Y.Q., Hover, D., Howell, J., Hung, T., Huppenkothen, D., Imel, D., Ip, W.H., Ivezić, Z., Jackson, E., Jones, L., Juric, M., Kasliwal, M.M., Kaspi, S., Kaye, S., Kelley, M.S.P., Kowalski, M., Kramer, E., Kupfer, T., Landry, W., Laher, R.R., Lee, C.D., Lin, H.W., Lin, Z.Y., Lunnan, R., Giomi, M., Mahabal, A., Mao, P., Miller, A.A., Monkewitz, S., Murphy, P., Ngeow, C.C., Nordin, J., Nugent, P., Ofek, E., Patterson, M.T., Penprase, B., Porter, M., Rauch, L., Rebbapragada, U., Reiley, D., Rigault, M., Rodriguez, H., Roestel, J.v., Rusholme, B., Santen, J.v., Schulze, S., Shupe, D.L., Singer, L.P., Soumagnac, M.T., Stein, R., Surace, J., Sollerman, J., Szkody, P., Taddia, F., Terek, S., Van Sistine, A., van Velzen, S., Vestrand, W.T., Walters, R., Ward, C., Ye, Q.Z., Yu, P.C., Yan, L., Zolkower, J., 2019. The Zwicky Transient Facility: System Overview, Performance, and First Results. *Publications of the Astronomical Society of the Pacific* 131, 018002. doi:[10.1088/1538-3873/aaecbe](https://doi.org/10.1088/1538-3873/aaecbe).
- Bertin, E., Arnouts, S., 1996. SExtractor: Software for source extraction. *Astronomy and Astrophysics Supplement Series* 117, 393–404. doi:[10.1051/aas:1996164](https://doi.org/10.1051/aas:1996164).
- Bosch, J., Armstrong, R., Bickerton, S., Furusawa, H., Ikeda, H., Koike, M., Lupton, R., Mineo, S., Price, P., Takata, T., Tanaka, M., Yasuda, N., AlSayyad, Y., Becker, A.C., Coulton, W., Coupon, J., Garmilla, J., Huang, S., Krughoff, K.S., Lang, D., Leauthaud, A., Lim, K.T., Lust, N.B., MacArthur, L.A., Mandelbaum, R., Miyatake, H., Miyazaki, S., Murata, R., More, S., Okura, Y., Owen, R., Swinbank, J.D., Strauss, M.A., Yamada, Y., Yamanoi, H., 2018. The Hyper Suprime-Cam software pipeline. *Publications of the Astronomical Society of Japan* 70, S5. doi:[10.1093/pasj/psx080](https://doi.org/10.1093/pasj/psx080), [arXiv:1705.06766](https://arxiv.org/abs/1705.06766).

- Boucaud, A., Huertas-Company, Marc, Heneka, C., Ishida, E.E.O., Sedaghat, N., de Souza, R.S., Moews, B., Dole, H., Castellano, M., Merlin, E., Roscani, V., Tramacere, A., Killedar, M., Trindade, A.M.M., 2020. Photometry of high-redshift blended galaxies using deep learning. *Monthly notices of the Royal Astronomical Society* 491, 2481–2495. URL: <https://academic-oup-com.ezproxy.princeton.edu/mnras/article-pdf/491/2/2481/31196214/stz3056.pdf>, doi:10.1093/mnras/stz3056.
- Burke, C.J., Aleo, P.D., Chen, Y.C., Liu, X., Peterson, J.R., Sembroski, G.H., Lin, J.Y.Y., 2019. Deblending and classifying astronomical sources with Mask R-CNN deep learning. *Monthly Notices of the Royal Astronomical Society* 490, 3952–3965. doi:10.1093/mnras/stz2845, arXiv:1908.02748.
- Combettes, P.L., Pesquet, J.C., 2008. A proximal decomposition method for solving convex variational inverse problems. *Inverse problems* URL: <http://iopscience.iop.org/article/10.1088/0266-5611/24/6/065014/meta>.
- Combettes, P.L., Pesquet, J.C., 2009. Proximal splitting methods in signal processing URL: <http://arxiv.org/abs/0912.3522>, arXiv:0912.3522.
- Dekany, R., Smith, R.M., Riddle, R., Feeney, M., Porter, M., Hale, D., Zolkower, J., Belicki, J., Kaye, S., Henning, J., Walters, R., Cromer, J., Delacroix, A., Rodriguez, H., Reiley, D.J., Mao, P., Hover, D., Murphy, P., Burruss, R., Baker, J., Kowalski, M., Reif, K., Mueller, P., Bellm, E., Graham, M., Kulkarni, S.R., 2020. The Zwicky Transient Facility: Observing System. *Publications of the Astronomical Society of the Pacific* 132, 038001. doi:10.1088/1538-3873/ab4ca2.
- Graham, M.J., Kulkarni, S.R., Bellm, E.C., Adams, S.M., Barbarino, C., Blagorodnova, N., Bodewits, D., Bolin, B., Brady, P.R., Cenko, S.B., Chang, C.K., Coughlin, M.W., Kishalay De, K., Eadie, G., Farnham, T.L., Feindt, U., Frackowiak, A., Fremling, C., Gezari, S., Ghosh, S., Goldstein, D.A., Golkhou, V.Z., Goobar, A., Ho, A.Y., Huppenkothen, D., Ivezić, v., Jones, R.L., Juric, M., Kaplan, D.L., Kasliwal, M.M., Kelley, M.S., Kupfer, T., Lee, C.D., Lin, H.W., Lunnan, R., Mahabal, A.A., Miller, A.A., Ngeow, C.C., Nugent, P., Ofek, E.O., Prince, T.A., Rauch, L., Van Roestel, J., Schulze, S., Singer, L.P., Sollerman, J., Taddia, F., Yan, L., Ye, Q.Z., Yu, P.C., Barlow, T., Bauer, J., Beck, R., Belicki, J., Biswas, R., Brinell, V., Brooke, T., Bue, B., Bulla, M., Burruss, R., Connolly, A., Cromer, J., Cunningham, V., Dekany, R., Delacroix, A., Desai, V., Duev, D.A., Feeney, M., Flynn, D., Frederick, S., Gal-Yam, A., Giomi, M., Groom, S., Hacopian, E., Hale, D., Helou, G., Henning, J., Hover, D., Hillenbrand, L.A., Howell, J., Hung, T., Imel, D., Ip, W.H., Jackson, E., Kaspi, S., Kaye, S., Kowalski, M., Kramer, E., Kuhn, M., Landry, W., Laher, R.R., Mao, P., Masci, F.J., Monkevitz, S., Murphy, P., Nordin, J., Patterson, M.T., Penprase, B., Porter, M., Rebbapragada, U., Reiley, D., Riddle, R., Rigault, M., Rodriguez, H., Rusholme, B., Van Santen, J., Shupe, D.L., Smith, R.M., Soumagnac, M.T., Stein, R., Surace, J., Szkody, P., Terek, S., Van Sistine, A., Van Velzen, S., Vestrand, W.T., Walters, R., Ward, C., Zhang, C., Zolkower, J., 2019. The Zwicky transient facility: Science objectives. *Publications of the Astronomical Society of the Pacific* 131, 1–23. doi:10.1088/1538-3873/ab006c.
- Hemmati, S., Huff, E., Nayyeri, H., Ferté, A., Melchior, P., Mobasher, B., Rhodes, J., Shahidi, A., Teplitz, H., 2022. Deblending Galaxies with Generative Adversarial Networks. *The Astrophysical Journal* 941, 141. doi:10.3847/1538-4357/aca1b8, arXiv:2211.04488.
- Ho, J., Jain, A., Abbeel, P., 2020. Denoising Diffusion Probabilistic Models. arXiv e-prints, arXiv:2006.11239 arXiv:2006.11239.
- Ivezić, Ž., Kahn, S.M., Tyson, J.A., Abel, B., Acosta, E., Allsman, R., Alonso, D., AlSayyad, Y., Anderson, S.F., Andrew, J., Angel, J.R.P., Angeli, G.Z., Ansari, R., Antilogus, P., Araujo, C., Armstrong, R., Arndt, K.T., Astier, P., Aubourg, É., Auza, N., Axelrod, T.S., Bard, D.J., Barr, J.D., Barrau, A., Bartlett, J.G., Bauer, A.E., Bauman, B.J., Baumont, S., Bechtol, E., Bechtol, K., Becker, A.C., Becla, J., Beldica, C., Bellavia, S., Bianco, F.B., Biswas, R., Blanc, G., Blazek, J., Blandford, R.D., Bloom, J.S., Bogart, J., Bond, T.W., Booth, M.T., Borgland, A.W., Borne, K., Bosch, J.F., Boutigny, D., Brackett, C.A., Bradshaw, A., Brandt, W.N., Brown, M.E., Bullock, J.S., Burchat, P., Burke, D.L., Cagnoli, G., Calabrese, D., Callahan, S., Callen, A.L., Carlin, J.L., Carlson, E.L., Chandrasekharan, S., Charles-Emerson, G., Chesley, S., Cheu, E.C., Chiang, H.F., Chiang, J., Chirino, C., Chow, D., Ciardi, D.R., Claver, C.F., Cohen-Tanugi, J., Cockrum, J.J., Coles, R., Connolly, A.J., Cook, K.H., Cooray, A., Covey, K.R., Cribbs, C., Cui, W., Cutri, R., Daly, P.N., Daniel, S.F., Daruich, F., Daubard, G., Daves, G., Dawson, W., Delgado, F., Dellapenna, A., de Peyster, R., de Val-Borro, M., Digel, S.W., Doherty, P., Dubois, R., Dubois-Felsmann, G.P., Durech, J., Economou, F., Eifler, T., Eracleous, M., Emmons, B.L., Fausti Neto, A., Ferguson, H., Figueroa, E., Fisher-Levine, M., Focke, W., Foss, M.D., Frank, J., Freemon, M.D., Gangler, E., Gawiser, E., Geary, J.C., Gee, P., Geha, M., Gessner, C.J.B., Gibson, R.R., Gilmore, D.K., Glanzman, T., Glick, W., Goldina, T., Goldstein, D.A., Goode-now, I., Graham, M.L., Gressler, W.J., Gris, P., Guy, L.P., Guyonnet, A., Haller, G., Harris, R., Hascall, P.A., Haupt, J., Hernandez, F., Herrmann, S., Hileman, E., Hoblitt, J., Hodgson, J.A., Hogan, C., Howard, J.D., Huang, D., Huffer, M.E., Ingraham, P., Innes, W.R., Jacoby, S.H., Jain, B., Jammes, F., Jee, M.J., Jenness, T., Jernigan, G., Jevremović, D., Johns, K., Johnson, A.S., Johnson, M.W.G., Jones, R.L., Juramy-Gilles, C., Jurić, M., Kalirai, J.S., Kallivayalil, N.J., Kalmbach, B., Kantor, J.P., Karst, P., Kasliwal, M.M., Kelly, H., Kessler, R., Kinnison, V., Kirkby, D., Knox, L., Kotov, I.V., Krabbandam, V.L., Krughoff, K.S., Kubánek, P., Kuczewski, J., Kulkarni, S., Ku, J., Kurita, N.R., Lage, C.S., Lambert, R., Lange, T., Langton, J.B., Le Guillou, L., Levine, D., Liang, M., Lim, K.T., Lintott, C.J., Long, K.E., Lopez, M., Lotz, P.J., Lupton, R.H., Lust, N.B., MacArthur, L.A., Mahabal, A., Mandelbaum, R., Markiewicz, T.W., Marsh, D.S., Marshall, P.J., Marshall, S., May, M., McKercher, R., McQueen, M., Meyers, J., Migliore, M., Miller, M., Mills, D.J., Miraval, C., Moeyens, J., Moolekamp, F.E., Monet, D.G., Moniez, M., Monkevitz, S., Montgomery, C., Morrison, C.B., Mueller, F., Muller, G.P., Muñoz Arancibia, F., Neill, D.R., Newbry, S.P., Nief, J.Y., Nomerotki, A., Nordby, M., O'Connor, P., Oliver, J., Olivier, S.S., Olsen, K., O'Mullane, W., Ortiz, S., Osier, S., Owen, R.E., Pain, R., Palecek, P.E., Parejko, J.K., Parsons, J.B., Pease, N.M., Peterson, J.M., Peterson, J.R., Petravick, D.L., Libby Petrick, M.E., Petry, C.E., Pierfederici, F., Pietrowicz, S., Pike, R., Pinto, P.A., Plante, R., Plate, S., Plutchak, J.P., Price, P.A., Prouza, M., Radeka, V., Rajagopal, J., Rasmussen, A.P., Regnault, N., Reil, K.A., Reiss, D.J., Reuter, M.A., Ridgway, S.T., Riot, V.J., Ritz, S., Robinson, S., Roby, W., Roodman, A., Rosing, W., Roucelle, C., Rummel, M.R., Russo, S., Saha, A., Sassolas, B., Schalk, T.L., Schellart, P., Schindler, R.H., Schmidt, S., Schneider, D.P., Schneider, M.D., Schoening, W., Schumacher, G., Schwamb, M.E., Seab, J., Selvy, B., Sembroski, G.H., Seppala, L.G., Serio, A., Serrano, E., Shaw, R.A., Shipsey, I., Sick, J., Silvestri, N., Slater, C.T., Smith, J.A., Smith, R.C., Sobhani, S., Soldahl, C., Storrie-Lombardi, L., Stover, E., Strauss, M.A., Street, R.A., Stubbs, C.W., Sullivan, I.S., Sweeney, D., Swinbank, J.D., Szalay, A., Takacs, P., Tether, S.A., Thaler, J.J., Thayer, J.G., Thomas, S., Thornton, A.J., Thukral, V., Tice, J., Trilling, D.E., Turri, M., Van Berg, R., Vanden Berk, D., Vetter, K., Virieux, F., Vucina, T., Wahl, W., Walkowicz, L., Walsh, B., Walter, C.W., Wang, D.L., Wang, S.Y., Warner, M., Wiecha, O., Willman, B., Winters, S.E., Wittman, D., Wolff,

- S.C., Wood-Vasey, W.M., Wu, X., Xin, B., Yoachim, P., Zhan, H., 2019. LSST: From Science Drivers to Reference Design and Anticipated Data Products. *The Astrophysical Journal* 873, 111. doi:[10.3847/1538-4357/ab042c](https://doi.org/10.3847/1538-4357/ab042c), [arXiv:1808.07445](https://arxiv.org/abs/1808.07445).
- Joseph, R., Courbin, F., Starck, J.L., 2016. Multi-band morpho-Spectral Component Analysis Deblending Tool (MuSCADeT): Deblending colourful objects. *Astronomy and Astrophysics* 589, A2. doi:[10.1051/0004-6361/201527923](https://doi.org/10.1051/0004-6361/201527923), [arXiv:1603.00473](https://arxiv.org/abs/1603.00473).
- Lanusse, F., Melchior, P., Moolekamp, F., 2019. Hybrid Physical-Deep learning model for astronomical inverse problems URL: <http://arxiv.org/abs/1912.03980>, [arXiv:1912.03980](https://arxiv.org/abs/1912.03980).
- Lupton, R.H., 2005. Sdss image processing i : The deblender. URL: <https://api.semanticscholar.org/CorpusID:85560178>.
- MacCrann, N., Becker, M.R., McCullough, J., Amon, A., Gruen, D., Jarvis, M., Choi, A., Troxel, M.A., Sheldon, E., Yanny, B., Herner, K., Dodelson, S., Zuntz, J., Eckert, K., Rollins, R.P., Varga, T.N., Bernstein, G.M., Gruendl, R.A., Harrison, I., Hartley, W.G., Sevilla-Noarbe, I., Pieres, A., Bridle, S.L., Myles, J., Alarcon, A., Everett, S., Sánchez, C., Huff, E.M., Tarsitano, F., Gatti, M., Secco, L.F., Abbott, T.M.C., Aguena, M., Allam, S., Annis, J., Bacon, D., Bertin, E., Brooks, D., Burke, D.L., Carnero Rosell, A., Carrasco Kind, M., Carretero, J., Costanzi, M., Crocce, M., Pereira, M.E.S., De Vicente, J., Desai, S., Diehl, H.T., Dietrich, J.P., Doel, P., Eifler, T.F., Ferrero, I., Ferté, A., Flaugher, B., Fosalba, P., Frieman, J., García-Bellido, J., Gaztanaga, E., Gerdes, D.W., Giannantonio, T., Gschwend, J., Gutierrez, G., Hinton, S.R., Hollowood, D.L., Honscheid, K., James, D.J., Lahav, O., Lima, M., Maia, M.A.G., March, M., Marshall, J.L., Martini, P., Melchior, P., Menanteau, F., Miquel, R., Mohr, J.J., Morgan, R., Muir, J., Ogando, R.L.C., Palmese, A., Paz-Chinchón, F., Plazas, A.A., Rodríguez-Monroy, M., Roodman, A., Samuroff, S., Sanchez, E., Scarpine, V., Serrano, S., Smith, M., Soares-Santos, M., Suchyta, E., Swanson, M.E.C., Tarle, G., Thomas, D., To, C., Wilkinson, R.D., Wilkinson, R.D., DES Collaboration, 2022. Dark Energy Survey Y3 results: blending shear and redshift biases in image simulations. *Monthly Notices of the Royal Astronomical Society* 509, 3371–3394. doi:[10.1093/mnras/stab287010.48550/arXiv.2012.08567](https://doi.org/10.1093/mnras/stab287010.48550/arXiv.2012.08567), [arXiv:2012.08567](https://arxiv.org/abs/2012.08567).
- Mandelbaum, R., 2018. Weak Lensing for Precision Cosmology. *Annual Review of Astronomy and Astrophysics* 56, 393–433. doi:[10.1146/annurev-astro-081817-05192810.48550/arXiv.1710.03235](https://doi.org/10.1146/annurev-astro-081817-05192810.48550/arXiv.1710.03235), [arXiv:1710.03235](https://arxiv.org/abs/1710.03235).
- Melchior, P., Joseph, R., Moolekamp, F., 2019. Proximal adam: Robust adaptive update scheme for constrained optimization. *arXiv e-prints*, [arXiv:1910.10094](https://arxiv.org/abs/1910.10094) URL: <https://ui.adsabs.harvard.edu/abs/2019arXiv191010094M>.
- Melchior, P., Joseph, R., Sanchez, J., MacCrann, N., Gruen, D., 2021. The challenge of blending in large sky surveys. *Nature Reviews Physics* 3, 712–718. doi:[10.1038/s42254-021-00353-y](https://doi.org/10.1038/s42254-021-00353-y).
- Melchior, P., Moolekamp, F., Jerdee, M., Armstrong, R., Sun, A.L., Bosch, J., Lupton, R., 2018. SCARLET: Source separation in multi-band images by Constrained Matrix Factorization. *Astronomy and Computing* 24, 129. doi:[10.1016/j.ascom.2018.07.001](https://doi.org/10.1016/j.ascom.2018.07.001), [arXiv:1802.10157](https://arxiv.org/abs/1802.10157).
- Mendoza, I., . Blendingtoolkit. URL: <https://lsstdesc.org/BlendingToolkit/index.html>.
- Moolekamp, F., Melchior, P., 2018. Block-simultaneous direction method of multipliers: a proximal primal-dual splitting algorithm for nonconvex problems with multiple constraints. *Optimization and Engineering. International Multidisciplinary Journal to Promote Optimization Theory & Applications in Engineering Sciences* URL: <https://doi.org/10.1007/s11081-018-9380-y>, doi:[10.1007/s11081-018-9380-y](https://doi.org/10.1007/s11081-018-9380-y).
- Nichol, A., Dhariwal, P., 2021. Improved Denoising Diffusion Probabilistic Models. *arXiv e-prints*, [arXiv:2102.09672](https://arxiv.org/abs/2102.09672), [arXiv:2102.09672](https://arxiv.org/abs/2102.09672).
- Nourbakhsh, E., Tyson, J.A., Schmidt, S.J., LSST Dark Energy Science Collaboration, 2022. Galaxy blending effects in deep imaging cosmic shear probes of cosmology. *Monthly Notices of the Royal Astronomical Society* 514, 5905–5926. doi:[10.1093/mnras/stac130310.48550/arXiv.2112.07659](https://doi.org/10.1093/mnras/stac130310.48550/arXiv.2112.07659), [arXiv:2112.07659](https://arxiv.org/abs/2112.07659).
- Parikh, N., Boyd, S., 2014. Proximal algorithms. *Foundations and Trends® in Optimization* 1, 127–239. URL: <http://dx.doi.org/10.1561/2400000003>, doi:[10.1561/2400000003](https://doi.org/10.1561/2400000003).
- Reiman, D.M., Göhre, B.E., 2019. Deblending galaxy superpositions with branched generative adversarial networks. *Monthly Notices of the Royal Astronomical Society* 485, 2617–2627. doi:[10.1093/mnras/stz575](https://doi.org/10.1093/mnras/stz575), [arXiv:1810.10098](https://arxiv.org/abs/1810.10098).
- Rowe, B.T.P., Jarvis, M., Mandelbaum, R., Bernstein, G.M., Bosch, J., Simet, M., Meyers, J.E., Kacprzak, T., Nakajima, R., Zuntz, J., Miyatake, H., Dietrich, J.P., Armstrong, R., Melchior, P., Gill, M.S.S., 2015. GALSIM: The modular galaxy image simulation toolkit. *Astronomy and Computing* 10, 121–150. doi:[10.1016/j.ascom.2015.02.002](https://doi.org/10.1016/j.ascom.2015.02.002), [arXiv:1407.7676](https://arxiv.org/abs/1407.7676).
- Sampson, M.L., Melchior, P., 2023. Spotting Hallucinations in Inverse Problems with Data-Driven Priors. *arXiv e-prints*, [arXiv:2306.13272](https://arxiv.org/abs/2306.13272) doi:[10.48550/arXiv.2306.13272](https://doi.org/10.48550/arXiv.2306.13272), [arXiv:2306.13272](https://arxiv.org/abs/2306.13272).
- Smith, L.N., Topin, N., 2017. Super-Convergence: Very fast training of neural networks using large learning rates URL: <http://arxiv.org/abs/1708.07120>, [arXiv:1708.07120](https://arxiv.org/abs/1708.07120).
- Smith, M.J., Geach, J.E., Jackson, R.A., Arora, N., Stone, C., Courteau, S., 2022. Realistic galaxy image simulation via score-based generative models. *Monthly Notices of the Royal Astronomical Society* 511, 1808–1818. doi:[10.1093/mnras/stac130.48550/arXiv.2111.01713](https://doi.org/10.1093/mnras/stac130.48550/arXiv.2111.01713), [arXiv:2111.01713](https://arxiv.org/abs/2111.01713).
- Song, Y., Ermon, S., 2019. Generative modeling by estimating gradients of the data distribution. *Advances in Neural Information Processing Systems* 32.
- Song, Y., Ermon, S., 2020. Improved Techniques for Training Score-Based Generative Models. *arXiv e-prints*, [arXiv:2006.09011](https://arxiv.org/abs/2006.09011), [arXiv:2006.09011](https://arxiv.org/abs/2006.09011).
- Song, Y., Sohl-Dickstein, J., Kingma, D.P., Kumar, A., Ermon, S., Poole, B., 2020. Score-Based Generative Modeling through Stochastic Differential Equations. *arXiv e-prints*, [arXiv:2011.13456](https://arxiv.org/abs/2011.13456), [arXiv:2011.13456](https://arxiv.org/abs/2011.13456).
- Wang, H., Sreejith, S., Slosar, A., Lin, Y., Yoo, S., 2022. Galaxy deblending using residual dense neural networks. *Physical Review D* 106, 063023. doi:[10.1103/PhysRevD.106.063023](https://doi.org/10.1103/PhysRevD.106.063023), [arXiv:2109.09550](https://arxiv.org/abs/2109.09550).
- Ward, C., Gezari, S., Nugent, P., Kerr, M., Eracleous, M., Frederick, S., Hammerstein, E., Graham, M.J., van Velzen, S., Kasliwal, M.M., Laher, R.R., Masci, F.J., Purdum, J., Racine, B., Smith, R., 2023. Panic at the ISCO: time-varying double-peaked broad lines from evolving accretion disks are common amongst optically variable AGN. *arXiv e-prints*, [arXiv:2309.02516](https://arxiv.org/abs/2309.02516) doi:[10.48550/arXiv.2309.02516](https://doi.org/10.48550/arXiv.2309.02516), [arXiv:2309.02516](https://arxiv.org/abs/2309.02516).

6. Appendix

6.1. Simulated priors

As we state in [Section 2](#), SCARLET2 allows for user-defined prior distributions, for which a neural network will then be trained to generate the gradient of the log prior of the distribution. While in some cases there will

exist readily available datasets suitable to be used as a galaxy morphology prior this will not always be true. One approach would then be to perform an initial *rough* deblending of the dataset using a pre-existing deblending tool, such as SCARLET 1 itself. However, if one has a reasonably good estimation about what the prior may be then it would likely be more sensible to create a mock prior distribution using simulation tools such as GALSIM. We provide an example result of the latter approach for an assumed prior of the Zwicky Transient Facility (ZTF). The simulated dataset is described in Section 3.1.

We test this model by fitting multi-band ZTF images of a single galaxy. We begin with a basic Gaussian initialization for the source at the location of the galaxy (Figure 12a) and obtain a high-quality model despite the low ($1.0''$) resolution and S/N of the ZTF images (Figure 12b). We also repeat the modeling for the case where imaging in all bands had a rectangle of central pixels with zero weights, imitating a masked region due to an artifact, and find that an accurate model is still produced (Figure 12c). These sample results show that using simulated morphology priors can result in robust, and accurate deblending where we note that no true model initialization has been needed or used in these three trials. This shows that our tool can be adapted to suit not just large, data-heavy surveys, but to a wide range of applications even with limited data availability.

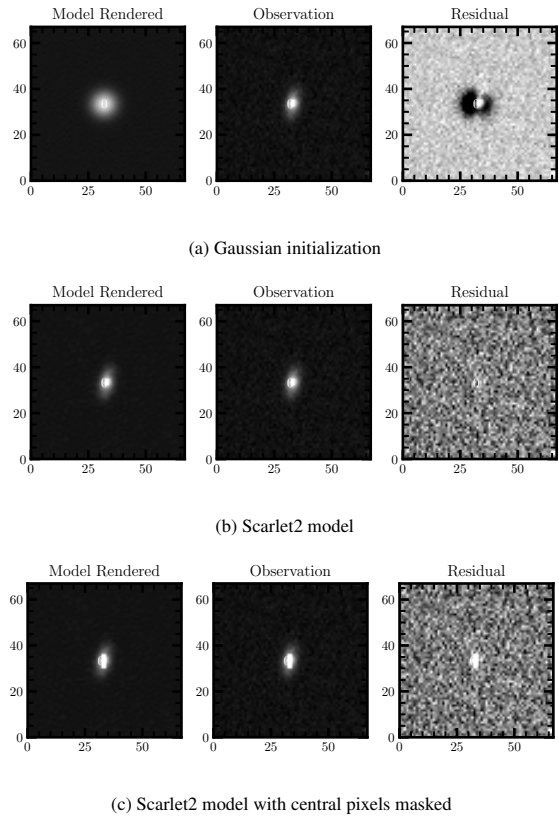


Figure 12: Images, SCARLET2 models, and residuals from testing of the custom ZTF prior on multi-band ZTF cutouts. The galaxy was initialized as a Gaussian and SCARLET2 was used with the ZTF prior to produce a model for an unmasked set of images (b) and a set of images in which all bands had a rectangle of masked pixels in the galaxy center (c). The central masked pixels are shown in white in image c). We show grayscale images for one of the three bands for clarity.